JOURNAL OF PROPULSION AND POWER
Vol. 12, No. 1, January–February 1996

Reacting Flow Simulation for a Large-Scale Ram Accelerator

Michael J. Nusca* and David L. Kruczynski†
U.S. Army Research Laboratory, Aberdeen Proving Ground, Maryland 21005

Computational fluid dynamics solutions of the full Navier–Stokes equations have been used to numerically simulate the reacting in-bore flowfield for the ram accelerator projectile propulsion system. In this system a projectile and obturator are injected at supersonic velocity into a stationary tube filled with a pressurized mixture of hydrocarbon, oxidizer, and inert gases. Flow stagnation on the obturator initiates combustion of the mixture, before it is discarded. A system of shock waves on the projectile, in conjunction with viscous heating, sustains combustion. The resulting energy release, which travels with the projectile, also generates high pressures that impart thrust to the projectile. Numerical simulation utilizing finite rate chemical kinetics have been used to investigate this flowfield. Numerical results are used to visualize the flowfield, predict the effects of variation in system parameters, and predict projectile in-bore velocity.

Nomenclature

b = covolume
C = specific reaction rate constant
c_p = specific heat capacity, constant p
c_v = specific heat capacity, constant volume
D = mass diffusion coefficient
E_a = activation energy
e = specific total internal energy
$\mathbf{F}, \mathbf{G}$ = flux vectors, Eq. (1)
g = Gibbs energy per mole
h = molar specific enthalpy
i = ith species
L = total length of projectile
$\mathcal{M}$ = molecular weight
m = mixture quantity
N = total number of species
n = number of moles
Pr = Prandtl number
p = static pressure
Q = heat content of the mixture
$\mathcal{R}$ = specific gas constant, $(\gamma - 1)c_p/\gamma$
$\bar{\mathcal{R}}$ = universal gas constant, $\mathcal{R}\mathcal{M}_m$
Sc = Schmidt number, $\mu_m/\rho D$
T = static temperature
t = time
U = magnitude of the local velocity vector
u = axial velocity
V = specific volume, $1/\rho$
v = radial velocity
$\mathbf{W}$ = dependent variable vector, Eq. (1)
X = species mole fraction
x, y = Cartesian coordinates
α = 0 (two-dimensional), 1 (axisymmetric)
γ = ratio of specific heats, c_p/c_v
ΔH_f = enthalpy of formation
κ = heat transfer coefficient
μ = molecular viscosity
ν = stoichiometric coefficient
ρ = density
σ = species mass fraction
τ = shear stress tensor
$\mathbf{\Omega}$ = source term vector, Eq. (1)
ω = chemical production term, Eq. (19)

Introduction

EXPERIMENTAL testing and gasdynamic modeling of the ram acceleration technique for in-bore projectile propulsion is being investigated at the U.S. Army Research Laboratory (ARL) under the Hybrid Inbore RAM (HIRAM) propulsion program.[1–5] This research program seeks to provide a highly efficient method of achieving hypervelocity (≥3 km/s) projectile gun-launch for use in high-speed impact testing applications. The ARL ram accelerator system uses a 120-mm (bore diameter) tube that is modeled after the 38-mm system at the University of Washington[6] where the technology was first demonstrated. Ram acceleration technology has also been successfully demonstrated at the Institute of St. Louis (ISL) in France.[7,8]

Numerical solutions of the Navier–Stokes equations have been obtained at the ARL via computational fluid dynamics (CFD) for nonreacting and reacting, two- and three-dimensional flows. These codes are being used to investigate the complex gasdynamic physics of ram accelerator projectile propulsion. A variety of CFD techniques have been brought to bear on this problem, including models for chemically frozen (nonreacting) gas, finite rate global and multiple-step chemical kinetics, and equilibrium chemical processes. Accurate numerical simulation of hydrocarbon-based reacting flow creates a very great demand on computational resources since the number of intermediate species and the number of kinetic steps for typical hydrocarbon fuels are prohibitively large. Global reaction mechanisms based on up to three steps have therefore been investigated for use in preliminary design studies. Within several hours on supercomputers, viscous and chemically reacting gasdynamic simulations are used to assess the influence of projectile velocity, tube fill pressure and mixture composition, and projectile geometry on species consumption, tube wall pressure and projectile thrust. These studies are being used to seek optimum performance for the ARL ram accelerator with minimal gun firings.

The ARL ram accelerator facility, projectile, operation, and experimental results are reviewed by Kruczynski[1,2] and therefore are not repeated here.

Received Aug. 27, 1993; revision received April 10, 1995; accepted for publication April 13, 1995.

[*] Aerospace Engineer, Weapons Technology Directorate. Senior Member AIAA.

[†] Mechanical Engineer, Weapons Technology Directorate. Member AIAA.

Reacting Flow Model

CFD flow simulations for the ARL ram accelerator are performed using the Rockwell Science Center unified solution algorithm real gas (USA-RG) code.[9–11] This CFD code solves the full, three-dimensional, unsteady Reynolds-averaged Navier–Stokes (RANS) equations including equations for chemical kinetics (finite rate and equilibrium). These partial differential equations are cast in conservation form and converted to algebraic equations using an upwind finite volume formulation. Solution takes place on a mesh of nodes distributed in a zonal fashion around the projectile and throughout the flowfield such that sharp geometric corners and other details are accurately represented. The conservation law form of the equations assures that the end states of regions of discontinuity (shocks, detonations, and deflagrations) are physically correct, even when smeared over a few computational cells. The total variation diminishing (TVD) technique is employed to discretize inertia terms of the conservation equations, whereas the viscous terms are evaluated using an unbiased stencil. Flux computations across cell boundaries are based on Roe's scheme for hyperbolic equations.[12] Spatial accuracy of third-order can be maintained in regions of the flowfield with continuous variation, whereas slope limiting, used near large flow gradients, reduces the accuracy locally to avoid spurious oscillations.

Previous investigators have used CFD to simulate ram accelerator flowfields. In each case CFD was used to solve the Navier–Stokes equations for the chemically reacting flowfield in the accelerator tube, around the projectile. Differences in CFD analysis arise from choices of numerical solution/discretization algorithm, representation of the turbulence terms, equation of state, and chemical kinetics scheme. Soetrisno et al.[13] used the lower-upper sucessive Gauss–Seidel (LU-SGS) implicit finite volume method (flux-vector splitting and symmetric TVD) with an approximate diagonal chemical source term Jacobian, algebraic turbulence model, perfect-gas equation of state, and a quasi-global, 9-species/12-reaction, methane–oxygen finite rate kinetics model. Yunster et al.[14] used the lower–upper steady successive over-relaxation (LU-SSOR) implicit finite volume method (implicit factorization and symmetric TVD) with a full chemical source term Jacobian, algebraic turbulence model, perfect-gas equation of state, and a 20-species/52-reaction, finite rate kinetics model. Li et al.[15] used the flux-corrected transport (FCT) explicit finite volume method with a non-inertial source term to account for projectile acceleration, inviscid flow model, perfect-gas equation of state, and a simplified two-step parametric hydrogen–air kinetics model (induction step followed by energy release step). Hosangadi et al.[16] used the Roe/TVD upwind implicit finite volume method (Riemann scheme modified for multiphase flows) with a fully coupled chemical source term Jacobian, two-equation and large-eddy turbulence models, virial equation of state, and a quasiglobal, 9-species/12-reaction finite rate kinetics model.

The RANS equations for two-dimensional/axisymmetric reacting flow (N species mixture) are written in the following conservation form[11]:

$$\frac{\partial \boldsymbol{W}}{\partial t} + \frac{\partial(\boldsymbol{F}_1 - \boldsymbol{G}_1)}{\partial x} + \frac{\partial(\boldsymbol{F}_2 - \boldsymbol{G}_2)}{\partial y} \frac{\alpha(\boldsymbol{F}_2 - \boldsymbol{G}_2)}{y} = \boldsymbol{\Omega} \quad (1)$$

$$\boldsymbol{W} = \begin{bmatrix} e \\ \rho \\ \rho u \\ \rho v \\ \rho\sigma_1 \\ \vdots \\ \rho\sigma_{N-1} \end{bmatrix}, \quad \boldsymbol{F}_1 = \begin{bmatrix} (e + p)u \\ \rho u \\ \rho u^2 + p \\ \rho uv \\ \rho u\sigma_1 \\ \vdots \\ \rho u\sigma_{N-1} \end{bmatrix}$$

$$\boldsymbol{F}_2 = \begin{bmatrix} (e + p)v \\ \rho v \\ \rho vu \\ \rho v^2 + p \\ \rho v\sigma_1 \\ \vdots \\ \rho v\sigma_{N-1} \end{bmatrix}, \quad \boldsymbol{\Omega} = \begin{bmatrix} 0 \\ 0 \\ 0 \\ \alpha\tau_+ \\ \sum\limits_k \omega_{1k} \\ \vdots \\ \sum\limits_k \omega_{(N-1)k} \end{bmatrix}$$

Viscous stress, heat conduction, and mass diffusion terms are given in arrays $\boldsymbol{G}_1$ and $\boldsymbol{G}_2$ (see Ref. 3). The species viscosity and thermal conductivity are referenced to μ_0, κ_0, and T_0 using Sutherland's law

$$\frac{\mu_i}{\mu_{0_i}} = \left(\frac{T}{T_{0\mu}}\right)^{3/2} \frac{T_{0\mu} + S_\mu}{T + S_\mu}, \qquad \frac{\kappa_i}{\kappa_{0_i}} = \left(\frac{T}{T_{0\kappa}}\right)^{3/2} \frac{T_{0\kappa} + S_\kappa}{T + S_\kappa} \quad (2)$$

where T_0 and S vary with species.[17] The mixture viscosity and thermal conductivity are determined using Wilke's law[18] denoting f as μ or κ

$$f_m = \sum_{i=1}^{N} \left[X_i f_i \left(\sum_{j=1}^{N} X_j \phi_{ij} \right)^{-1} \right]$$
$$\phi_{i,j} = \frac{1}{\sqrt{8}} \left(1 + \frac{\mathcal{M}_i}{\mathcal{M}_j}\right)^{-1/2} \left[1 + \left(\frac{f_i}{f_j}\right)^{1/2} \left(\frac{\mathcal{M}_j}{\mathcal{M}_i}\right)^{1/4}\right]^2 \quad (3)$$

Fick's law is used to relate the mixture diffusivity to the mixture viscosity through $Sc = \mu_m/(\rho D)$. The specific heat, enthalpy, and Gibbs free energy of each species (per mass) are given by the following fourth-order polynomial curve fits in terms of temperature T (Ref. 19):

$$\frac{c_{p_i}}{\mathcal{R}_i} = A_i + B_i T + C_i T^2 + D_i T^3 + E_i T^4 \quad (4)$$

$$h_i = \mathcal{R}_i \left(A_i + \frac{B_i}{2} T + \frac{C_i}{3} T^2 + \frac{D_i}{4} T^3 + \frac{E_i}{5} T^4 \right) T + \Delta H_{f_i} \quad (5)$$

$$\frac{g_i}{\mathcal{R}_i} = A_i(T - T \ln T) - \frac{B_i}{2} T^2 - \frac{C_i}{6} T^3 - \frac{D_i}{12} T^4$$
$$- \frac{E_i}{20} T^5 + \frac{\Delta H_{f_i}}{\mathcal{R}_i} - F_i T \quad (6)$$

The mixture enthalpy, total energy per unit volume, and ratio of specific heats are given by

$$h = \sum_{i=1}^{N} \sigma_i \int^{T} c_{p_i} \, \mathrm{d}T + \sum_{i=1}^{N} \sigma_i \Delta H_{f_i}$$
$$e = \frac{p}{\gamma - 1} + \rho \frac{(u^2 + v^2)}{2} + \sum_{i=1}^{N} \rho\sigma_i \Delta H_{f_i} \quad (7)$$

$$\gamma = 1 + \left[\frac{c_{pm}}{\bar{\mathcal{R}} \sum\limits_i (\sigma_i/\mathcal{M}_i)} - 1 \right]^{-1}, \quad c_{pm} = \frac{1}{T} \sum_{i=1}^{N} \sigma_i \int^{T} c_{p_i} \, \mathrm{d}T \quad (8)$$

Equation of State

There exists a number of formulas that have been proposed to describe the thermodynamic behavior for states where the deviations from a perfect gas are distinct.[20] In most cases the improvement starts from the perfect gas concept as the limiting case for small pressures and large specific volumes, adapting the formulas according to the observed behavior by means of suitable corrections:

$$p = \sum_{i=1}^{N} p_i = \rho T \bar{\mathfrak{R}} \sum_{i=1}^{N} \frac{\sigma_i}{\mathcal{M}_i} \tag{9}$$

Some of the best known examples are given as follows:

$$\left(p + \frac{a}{V^2}\right)(V - b) = n\bar{\mathfrak{R}}T \qquad \text{(van der Waals)} \tag{10}$$

$$p(V - b) = n\bar{\mathfrak{R}}T, \qquad b = \sum_i n_i b_i \qquad \text{(Abel)} \tag{11}$$

$$\frac{pV}{n\bar{\mathfrak{R}}T} = 1 + \frac{B(T, n_i)}{V} + \frac{C(T, n_i)}{V^2} + \cdots \qquad \text{(Virial)} \tag{12}$$

Equations (10) and (11) are the simplest ways of taking into account the real gas effects using molecular attraction a and covolume b. Equation (11) can be derived from the Virial equation [Eq. (12)] assuming very high temperatures and gas densities low enough that the mean volume available per molecule is large compared to the volume of the hard-sphere core of the molecule.[21] Equation (12) is very general and, in principle, exactly valid. The convergence of the series, however, is guaranteed only for moderately dense gases. For high densities in chemically reacting flows the formula is practically of no use[20] unless the series is truncated and certain assumptions are made for B and C. Expressions for B and C, the second and third virial coefficients, are given by[22]

$$B = \sum_l \sum_m \sigma_l \sigma_m B_{lm}, \qquad C = \sum_l \sum_m \sum_n \sigma_l \sigma_m \sigma_n C_{lmn} \tag{13}$$

For a binary mixture these expressions reduce to

$$B = \sigma_1^2 B_{11} + 2\sigma_1\sigma_2 B_{12} + \sigma_2^2 B_{22}$$
$$C = \sigma_1^3 C_{111} + 3\sigma_1^2\sigma_2 C_{112} + 3\sigma_1\sigma_2^2 C_{122} + \sigma_2^3 C_{222}$$

Second and third pure coefficients (B_{11}, B_{22}, C_{111}, and C_{222}) as well as cross-coefficients (B_{12}, C_{112}, and C_{122}) are determined from experimental data that is, in general, available for only very limited applications.[22] Although B_{lm} and C_{lmn} are determinable in principle from intermolecular potential functions, these are rarely known accurately except for the simplest of molecules. The virial coefficients for pure species can be obtained experimentally from volumetric data, but those for species in solution are rarely available. It is thus usually necessary to postulate mixing rules relating the coefficients of the solution to the pure species. The main disadvantage of the Virial equation is its inapplicability to high densities.[23] Hosangadi et al.[16] used the Virial equation for ram accelerator flowfields and showed some effect in the location and strength of shock wave reflections. In these computations (for a multi-component hydrocarbon mixture) the cross-coefficients for B and all coefficients for C were neglected, thus, $C = 0$ and $B = \Sigma_l\, \sigma_l B_l$. For the computations described in the present work, a covolume equation of state is used [Eq. (11)], where b for each species is obtained from Hirschfelder.[24]

Turbulence Models

The system of Navier–Stokes equations is valid for the laminar flow of a viscous, Newtonian fluid. In reality, the flow will remain laminar up to a certain critical value of the Reynolds number, $\rho UL/\mu$, where U and L are representative values of the velocity and length scales for the considered flow system. Above this critical value the flow becomes turbulent and is characterized by the appearance of fluctuations in all variables (velocity, pressure, density, temperature, etc.), around mean values. These fluctuations are statistical in nature and cannot be described in a deterministic way. However, they can be computed numerically using approaches such as large eddy simulations (LES) and Reynolds-averaged Navier–Stokes (RANS) simulations. LES uses a fixed spacial resolution, with the effects of unresolved turbulent eddies modeled using gradient transport methods such as eddy viscosity. RANS model all turbulent fluctuations theoretically or empirically, not just the ones smaller than the computational grid spacing. The RANS equations are derived by decomposing the dependent variables in the conservation equations into time mean (obtained over an appropriate time interval) and fluctuating components and then time averaging the entire equation. This time averaging is defined in such a way as to remove the influence of the turbulent fluctuations while not destroying the time dependence associated with other time-dependent phenomena with time scales distinct from those of turbulence. After substitution of these variables into the mass, momentum, and energy conservation equations and cancelling terms that are identically zero, two types of stress terms are produced: 1) laminar-like stress gradients for the mean motion and 2) apparent stress gradients due to the transport of momentum by turbulent fluctuations. These apparent stresses are commonly called the Reynolds stresses. For first-order closure models the Reynolds stresses are expressed in terms of an eddy viscosity μ_t resulting from the Boussinesq assumption.[25] The Baldwin–Lomax model[26] describes the eddy viscosity using y_{max} as the value where Γ attains the value Γ_{max}, intermittency F, and constants $\alpha = 0.3$, $\beta = 1.6$, and $A = 26$:

$$\mu_t = 0.0168\beta F y_{\text{max}} \Gamma_{\text{max}}, \quad F = \left[1 + 5.5\left(\frac{\alpha y}{y_{\text{max}}}\right)^6\right]^{-1}$$
$$\Gamma = y(1 - e^{-y^+/A})|\nabla \times \bar{v}| \tag{14}$$

Where $y^+ = (y\rho/\mu)(\tau_{\text{wall}}/\rho)^{-1/2}$. This model has been used extensively for thin, attached shear layers at moderate Mach numbers with acceptable results. However, as soon as separation of the boundary layer is approached, poor predictions result. To improve the predictive capability of separated flows using RANS equations a new turbulence model has been developed.[27] The model is based on experimental observations of detached flows. The model prescribes turbulence kinetic energy and dissipation analytically within backflows. A formula for the eddy viscosity distribution within backflows is derived and used for the RANS equations when the calculations are done inside separation bubbles. Outside of them, the Baldwin–Lomax turbulence model[26] supplies the values of eddy viscosity. While the Baldwin–Lomax turbulence model is used to detect flow separation and to initiate application of the backflow model, the latter model can relocate the separation point.

Chemical Reactions

Hydrocarbon reactions are commonly used for ram accelerator testing at ARL,[1,2] e.g.,

$$3CH_4 + 2O_2 + 10N_2 \tag{15}$$

This reaction is one of a general class of hydrocarbon reactions investigated by Westbrook and Dryer[28]:

$$C_aH_bO_c + \tfrac{1}{2}[a + (b/2) + c]O_2 \Rightarrow aCO + (b/2)H_2O \tag{16}$$

The fuel equivalence ratio Φ is a measure of the amount of fuel available for combustion. When $\Phi = 1$, the proportions of fuel to oxygen are stoichiometric. For Φ values smaller than unity fuel should be completely consumed. For the reaction stated previously, $\Phi = 3.0$, which is considered outside

Table 1 Reaction rate equation data

Reaction	E_a	A	a	b	c	d	e	f
Eq. (17)	30.0	8.3×10^5	−0.3	1.3	0.0	0.0	1.0	2.0
Eq. (18), (1)	30.0	8.3×10^5	1.0	2.0	1.0	2.0	0.0	0.0
Eq. (18), (2)	44.7	3.0×10^6	0.0	0.5	1.0	0.0	1.0	0.0
Eq. (18), (3)	37.6	1.0×10^5	0.0	1.0	0.0	2.0	0.0	2.0

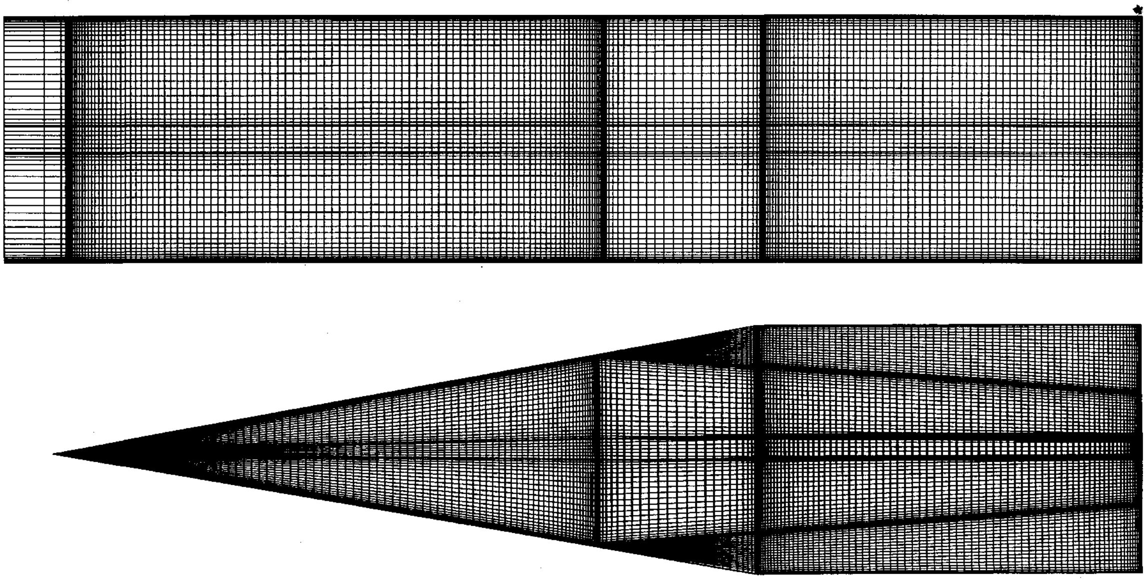

Fig. 1 Three-dimensional computational grid over surface of projectile with four fins (one fin hidden from view) and over surface of accelerator tube.

the range of well-understood CH_4/O_2 chemical kinetics especially for $P \geq 10$ atm.[29]

Including all intermediate species and reaction steps for Eq. (15) within the framework of a CFD calculation could be defeated by uncertainties in the thermodynamic, transport, and chemical-kinetic properties of these species, especially at high pressures where these data have not been measured. In addition, the computational cost of a given reaction mechanism depends primarily on the number of chemical species included, rather than the number of reactions.[28] Such extensive kinetic mechanisms (12–19 species) have been included in CFD analyses using atmospheric pressure kinetics data.[14] Given the previous concerns, global reaction mechanisms for hydrocarbon fuel and oxidizer (neglecting intermediate steps) have been proposed.[28,30] Using one-step chemistry

$$CH_4 + 2O_2 \Rightarrow CO_2 + 2H_2O \tag{17}$$

or assuming three-step chemistry

$$\begin{gathered} CH_4 + 2O_2 \Rightarrow CO + 2H_2 + 1.5O_2 \\ CO + 0.5O_2 \Rightarrow CO_2 \\ 2H_2 + O_2 \Rightarrow 2H_2O \end{gathered} \tag{18}$$

The reaction rate is defined using the law of mass action and an Arrhenius expression for C, the specific reaction rate constant:

$$\omega = C \prod_{i=1}^{N} \sigma_i^{\nu_i} = AT^{\alpha} \exp\left(\frac{-E_a}{\bar{\mathcal{R}}T}\right) \sigma_{CH_4}^{a} \sigma_{O_2}^{b} \sigma_{CO}^{c} \sigma_{H_2}^{d} \sigma_{CO_2}^{e} \sigma_{H_2O}^{f} \tag{19}$$

where AT^{α} is the collision frequency and the exponential term is the Boltzmann factor. The exponents α through f are given in Table 1.

Computational Grid

The governing equations, in finite volume form, are solved on a finite mesh of nodes distributed in a zonal fashion around the projectile and throughout the flowfield. Using this technique, sharp geometric corners and contour details are accurately represented. Figure 1 shows the projectile surface and tube surface for a three-dimensional mesh around the projectile. The number of axial, radial, and azimuthal grid nodes are 200, 25, and 66, respectively. Separate zones were placed ahead of the projectile nosetip, over the forebody, between the fins on the afterbody, and in the wake region. The mesh for an axisymmetric computation is simpler since the fins are removed, and therefore, only one azimuthal plane is required. Separate zones are generated as discussed earlier. Typically, the number of axial and radial grid nodes are 165 and 100, respectively.

Computational Results

Computational simulations for the ARL 120-mm ram accelerator were performed to validate the CFD code as well as investigate various gasdynamic and chemical kinetic effects. Results are presented in the following subsections. Some limited three-dimensional numerical simulations are presented in the first subsection. CFD code validation results, for axisymmetric flow, are presented in the second subsection where measured and computed tube wall pressures are compared. Time-accurate solutions are used to predict projectile performance and compared to measured data in the third subsection.

Steady Three Dimensional

Figure 2 shows the computed temperature contours on the projectile surface and accelerator tube surface for frozen (i.e., nonreacting) flow. The Mach number, tube charge pressure, and Reynolds number are 3.5, 51 atm, and 4.3×10^6, re-

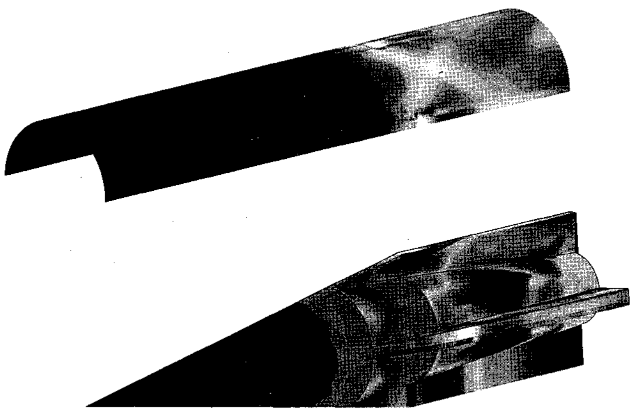

Fig. 2 Gray-scale surface temperature contours for three-dimensional projectile (one fin shown on edge) and tube wall. Frozen chemistry, $M = 3.5$, fill $p = 51$ atm, and fill $T = 298$ K. White = 1760 K and black = 394 K.

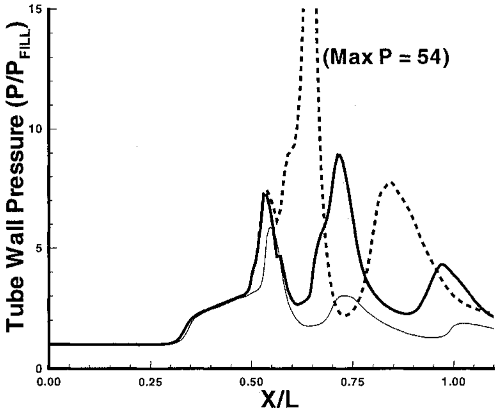

Fig. 3 Computed tube wall pressures, $M = 3.5$ and fill $p = 51$ atm. Axisymmetric (narrow line), three dimensional between fins (thick line), and three dimensional over fin tip (broken line).

spectively. In these gray-scale figures, the lighter colors correspond to hot temperatures. The forebody–afterbody junction is illustrated by a vertical black line ($0.5L$). Three fins are visible, top and bottom fins shown in the planform and the third fin shown on the edge (fin edges are illustrated by two horizontal black lines). Note the hot-gas temperature on the fin edge at the tip as well as on the tube surface where fin shocks intersect (whitish "X" patterns in Fig. 2). Gas temperatures on the forebody (cone) surface are uniform except where the nose shock intersects the projectile after reflecting from the tube wall. Several expansion regions and shock reflections can be observed along the fin planform (Fig. 2, top and bottom); a dark (cool) expansion region over the fin bevel, a bright (hot) shock impingement region at midplanform, and a succession of weakening (gray to black color) shock reflections along the fin. A dark (cool) flow expansion is also observed on the projectile afterbody between fins. The fin–fin shock interactions seen in the CFD simulation emulates experimental observations (see Fig. 5 of Kruczynski et al.[31] showing the experimental flow visualization via smear photograph where combustion is seen emanating from the fin leading edges and engulfing the projectile afterbody).

Figure 3 shows pressure distributions on the tube wall over the fin tip as well as between fins. High pressures at the fin tip ($x/L = 0.65$), between the fin and the tube wall (0.6 mm gap), as well as between the fins due to shock reflections and fin-shock intersections, are observed. Also shown in Fig. 3 is a comparison between pressure computed on the tube wall for a three-dimensional computation (between fins) and an axisymmetric computation (projectile without fins). Pressure peaks are observed in similar locations, but of reduced magnitude, for the axisymmetric case. These viscous, frozen chemistry, three-dimensional computations required 10 CPU hours (Cray 2). Computations with finite rate (three-step) kinetics required 15–20 CPU hours per case. Much can be learned by neglecting the projectile fins and investigating certain aspects of ram accelerator propulsion using axisymmetric simulations. These are the subject of the remainder of this section while further three-dimensional simulations will be addressed in future studies.

Steady Axisymmetric

CFD simulations were performed for conditions corresponding to shots 14, 15, 22, 23, and 25 of the ARL 120-mm ram accelerator.[2] While the gas mixture used for shot 14 consisted of nitrogen alone (i.e., inert shot), the other shots cited used the mixture described by Eq. (15). The projectile was accelerated to approximately 1200 m/s in each shot before entrance to the ram accelerator tube. This tube was pressurized to 750, 1000, 1250, and 1500 psi (51, 68, 85, and 102 atm), for shots 14/15, 22, 23, and 25, respectively (gas temperature of 298 K). Pressure taps were installed at 0.3, 0.6, 1.15, 2.3, 3.46, 4.06, and 4.35 m from the accelerator entrance diaphragm and will be hereafter referred to as stations 1–7. The velocity at each station was measured using a radar technique.[2]

Figures 4–8 show the comparison of measured and computed tube wall pressure distributions above the projectile at a particular tube station and for each shot (see Ref. 4 for further results). Figure 4 shows the results for the inert (chem-

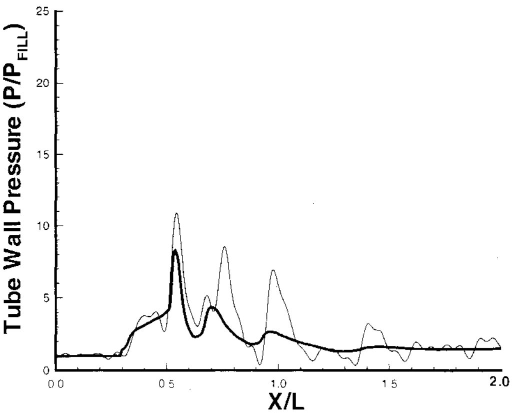

Fig. 4 Tube wall pressures, shot 14, station 5, inert flow, $M = 3.3$ and fill $p = 51$ atm. Measured (narrow line) and computed (thick line).

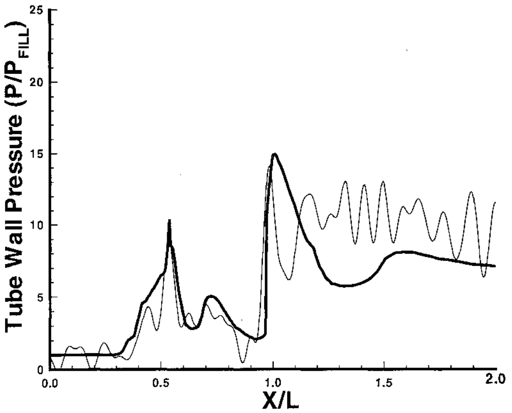

Fig. 5 Tube wall pressures, shot 15, station 4, $M = 3.45$ and fill $p = 51$ atm. Measured (narrow) and computed (thick line).

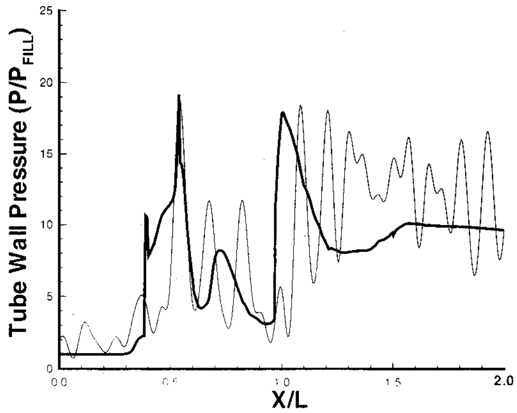

Fig. 6 Tube wall pressures, shot 22, station 4, M = 3.44, and fill p = 68 atm. Measured (narrow) and computed (thick line).

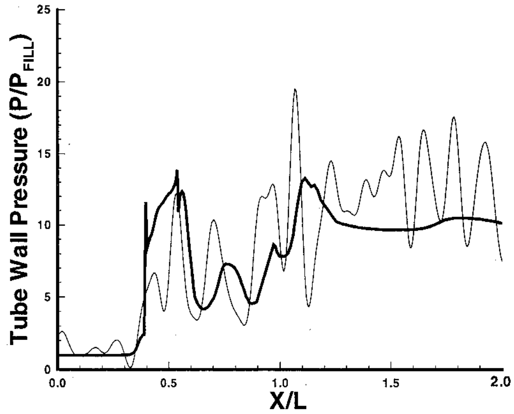

Fig. 7 Tube wall pressures, shot 23, station 4, M = 3.72, and fill p = 85 atm. Measured (narrow) and computed (thick line).

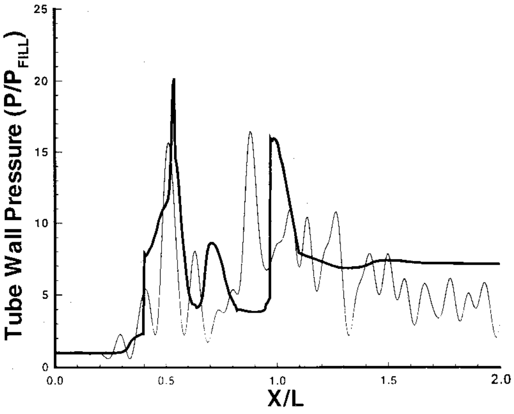

Fig. 8 Tube wall pressures, shot 25, station 1, M = 3.32, and fill p = 102 atm. Measured (narrow) and computed (thick line).

ically frozen) shot 14 using nitrogen gas. As noted in the comparison of three-dimensional and axisymmetric simulations (Fig. 3) locations of the pressure peaks agree with measurements, however, at a reduced magnitude. The trend in pressure peak magnitude with x/L is similar for computation and experiment. It should be noted that the obturator, not included in the computation, is in relatively close proximity to the projectile and could be affecting these pressures (shot 14 only). The relatively gradual obturator discard is a characteristic of inert shots not observed in shots through reacting mixtures.

Figure 5 shows data for station 4 and shot 15, the lowest pressure shot. The first substantial pressure rise ($x/L \simeq 0.55$) is slightly (5%) overpredicted. This peak is due to the first impact of the nose shock reflected from the tube wall to the projectile surface and back to the tube wall again. Computations indicate some level of reaction at this point.[4] The second predominant peak occurs nearly at the end of the projectile ($x/L = 1$) and is either predicted in the proper location or rearward; the magnitude in some cases is slightly over- or underpredicted. Pressures downstream of the projectile ($x/L > 1$) are generally computed near the measured magnitude, but without high oscillations. Several theories concerning the absense of pressure oscillations in these computations are under investigation, including the time-averaging technique and turbulence model employed.

Figures 6 and 7 show data and computations for shots 22 and 23, each representing subsequently higher tube fill pressures. Results for station 4 (middle of the tube) are shown and can be compared to station 4 (Fig. 5) for the low-pressure shot. The first major pressure rise ($x/L \simeq 0.55$) is preceded by a smaller pressure spike, to some degree replicated by the computation. More pressure spikes are recorded between $x/L = 0.55$ and $x/L = 1$ compared to shot 15. As with shot 15, large pressure rises occur near the end of the projectile ($x/L = 1$) and are simulated to a better degree for shot 22 (Fig. 6).

Figure 8 represents shot 25 using the highest tube fill pressure. Comparing this data (for station 1) with that for all other shots (for station 4) we find a trend toward similar magnitude for the first pressure spike, located near $x/L = 0.55$, and the second spike, located near $x/L = 1$. Both locations contain reacting flow and indicate combustion moving onto the forebody. Data recorded for subsequent stations[4] for shot 25 showed an unstart (i.e., combustion ahead of the projectile, see Kruczynski et al.[31]).

The discussion and conclusions presented previously are supported by flowfield visualization accomplished by plotting computed temperature fields for each shot. Figures 9 and 10 correspond to conditions for shot 14 station 5 (Mach = 3.3) and shot 15 station 4 (Mach = 3.45), respectively. In these gray-scale figures, the lighter colors correspond to cool temperatures. Figure 9, inert shot, shows the projectile nose shock reflecting from the tube wall, impinging near the projectile forebody/afterbody junction, and subsequently reflecting and weakening downstream. High-temperature boundary layers are observed on the projectile and tube walls. Figure 10, combustion shot, shows wide regions of high-temperature gas caused by shocks and combustion, superimposed. Note combustion occurs in the projectile and tube wall boundary layers as well; rapid boundary-layer thickening caused by shock wave impingment is evident. Some localized combustion occurs in the forebody boundary layer. Results for higher pressure shots[4] shows that extensive combustion between the projectile forebody and tube wall becomes more predominant with increasing freestream pressure. In addition, increased projectile acceleration causes the nose shock to reflect further rearward

Fig. 9 Gray-scale temperature contours, shot 14, station 5, inert flow, M = 3.3, and fill p = 51 atm. White = 298 K and black = 417 K.

Fig. 10 Gray-scale temperature contours, shot 15, station 4, M = 3.45, and fill p = 51 atm. White = 298 K and black = 745–2700 K.

on the tube wall, combustion to move from the second shock reflection to the first, and combustion in the forebody boundary layer to move forward. These effects shift high pressure to the forebody where drag is generated, counteracting thrust generated by high pressure on the afterbody.

Unsteady Axisymmetric

Time-accurate CFD simulations are reported for conditions corresponding to shot 27 of the ARL 120-mm ram accelerator.[2] The projectile was injected at approximately 1250 m/s (Mach number 3.5) into the accelerator tube filled with a gaseous mixture [see Eq. (15)] at 300 K and pressurized to 750 psi (50 atm). The mixture has a sound speed of 361 m/s, a Chapman–Jouget detonation speed of 1448 m/s, and a precombustion γ of 1.379 (see Ref. 5). Pressures on the accelerator tube wall were collected at 11 ports located from 0.3 to 9.1 m from the entrance diaphragm. Doppler radar was used to obtain a continuous in-bore velocity-time history of the projectile. The CFD simulation was started with entrance of the projectile/obturator combination into the accelerator tube at t = 20.05 ms with specified velocity (1256.4 m/s) and obturator back pressure (4000 psi). The projectile fins were neglected so that axisymmetric simulations could be used. The flowfield equations [Eq. (1)] were then solved in a time-accurate fashion along with a force computation for the projectile and obturator, individually. The velocity of the projectile and the relative separation between the projectile base and obturator were updated for each time step (0.2 ms) using the computed, time-dependent force and given masses. The backpressure on the obturator due to the conventional charge was assumed to be ambient after 20.45 ms. When the obturator is greater than five projectile lengths downstream of the projectile base, its influence on the projectile flowfield is negligible. A downstream outflow condition is then prescribed one projectile body length behind the projectile.

Figures 11 and 12 show the computed time sequence of projectile obturator separation in terms of gas H_2O mass fraction and flowfield Mach number, respectively. Water is a major product for the reaction given by Eqs. (17) and (18), thus illustrating regions of significant combustion activity. For Fig. 11, white corresponds to the absence of H_2O in the flowfield, while dark gray corresponds to a water mass fraction of 0.1. For Fig. 12, black corresponds to subsonic flow. Flow stagnation on the obturator, when in close proximity to the projectile, causes both a normal shock and a combustion front to occur on the projectile. The combustion front is located on the projectile forebody while the normal shock is located on the afterbody. Flow between the combustion front and the normal shock is slightly supersonic. As the obturator is pushed further back from the projectile (the last frame of Figs. 11 and 12 corresponds to an obturator location of 1.47 m or 2.81 projectile lengths, behind the projectile base), the normal shock moves rearward and is eventually positioned behind the projectile. At this point the projectile is in fully supersonic flight. Combustion occurs at the projectile-afterbody junction due to shock heating, in the projectile and tube wall boundary layers due to stagnation heating, and downstream of the normal shock traveling behind the projectile. This normal shock, which also initiates combustion, is now driven by the obturator (i.e., a piston). Because of the high combustion pressures on the side facing the projectile as well as the relieved backpressure, the obturator is moving slower than the projectile (this computational simulation can be compared to the experimentally photographed sequence portrayed in Figs. 4 and 6 of Kruczynski et al.[31]).

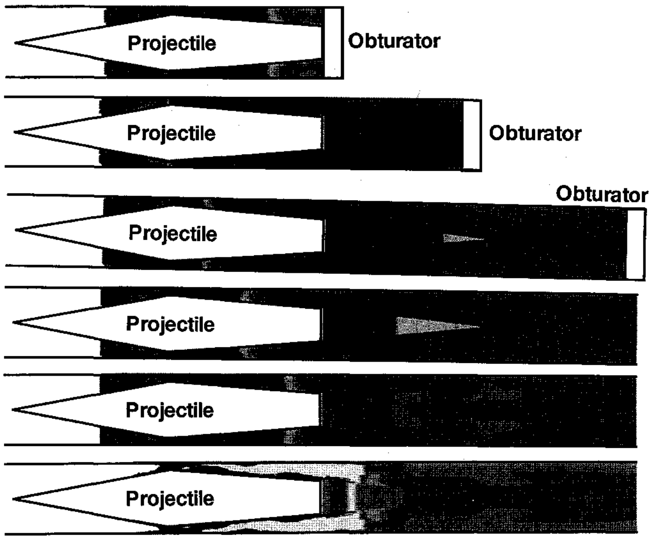

Fig. 11 **Flowfield H_2O mass fraction contours ($0 \leq \sigma \leq 0.1$). Standard mixture at 51 atm. Time sequence from 20.05 to 21.05, 0.2 ms interval. Computed projectile velocities: 1256, 1267, 1289, 1299, 1305, and 1310 m/s. Computed obturator locations: 0, 0.443, 0.961, 1.51, 2.1, and 2.81 m from projectile base.**

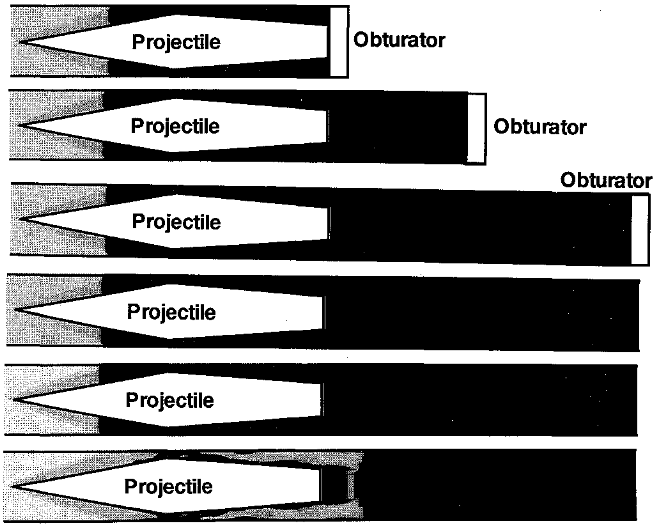

Fig. 12 **Flowfield Mach number contours ($0.09 \leq M \leq 3.9$). Standard mixture at 51 atm. Time sequence from 20.05 to 21.05, 0.2 ms interval. Computed projectile velocities: 1256, 1267, 1289, 1299, 1305, and 1310 m/s. Computed obturator locations: 0, 0.443, 0.961, 1.51, 2.1, and 2.81 m from projectile base.**

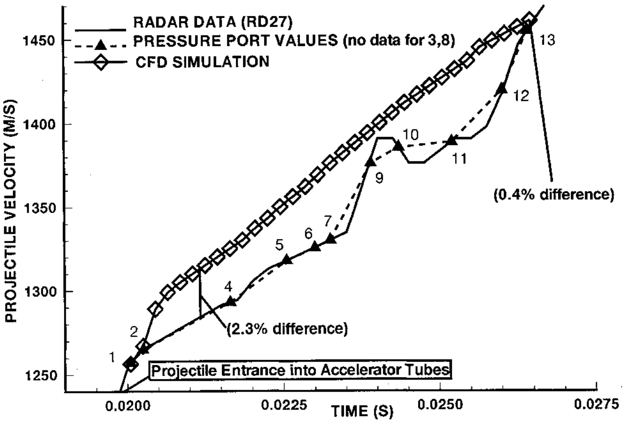

Fig. 13 **Computed and measured projectile velocity vs time of flight for shot 27. Mixture: $3CH_4 + 2O_2 + 10N_2$ at 51 atm and 300-K fill conditions.**

Figure 13 shows the measured projectile velocity-time history. The projectile velocity was measured using a Doppler radar positioned outside the accelerator and beamed down

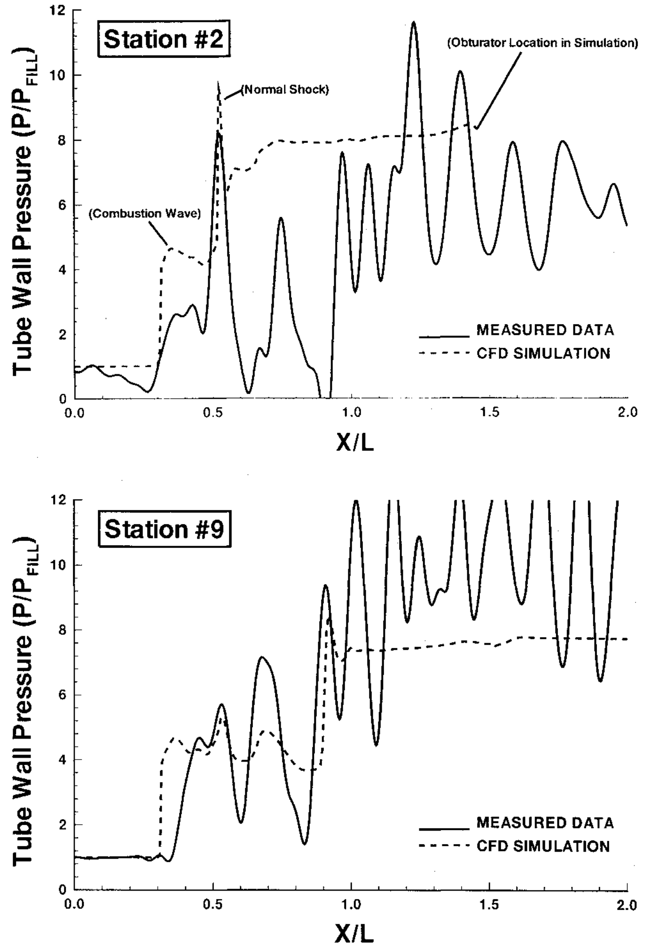

Fig. 14 Computed and measured tube wall pressure distributions for shot 27, station numbers 2 and 9.

the tube bore using a sacrificial mirror. Tube-mounted transducers were used to measured the projectile pressure signature as it passed each station. The computer simulation shows overprediction with respect to measurements, beyond station 2. Thereafter the computed projectile velocity was fairly constant at 2.3% above measurements. The large projectile thrust computed after station 2 is due to a higher than measured pressure on the projectile afterbody. It is thought that perhaps the obturator is tilted (i.e., the obturator length is such that the obturator can spin within the tube cross section), thus relieving pressure from behind the projectile. Figure 14 shows a comparison of the measured and computed tube wall pressure distribution at station 2. Figure 14 also shows results for station 9, where better agreement is obtained. A possible cause for discrepancy in computed pressures are flow transients introduced by diaphragm rupture that are not included in the simulation.

Conclusions

CFD simulations of the ram accelerator show that shock waves originating from the projectile nosetip and reflecting from the accelerator tube wall provide sufficient heating to sustain combustion of the gas mixture. Wall boundary layers on the projectile forebody and afterbody sections, as well as on the accelerator tube, provide locally reacting regions. On the afterbody, combustion is generally confined to these wall layers that thicken with distance. Unsteady simulations show stagnation of the combustible gas on the projectile obturator, which causes formation of a normal shock and a combustion wave in the flowfield. As the obturator is gasdynamically discarded, the normal shock trails behind the projectile and the combustion wave collapses into shock-induced combustion on the projectile. This effect has been observed computationally as well as with experimental flow visualization. With the obturator sufficiently downstream, the projectile accelerates at supersonic speeds. Projectile velocity through the accelerator can be adequately predicted.

Acknowledgments

A. Horst, T. Minor, and D. Kooker have supported both the experimental and numerical simulation aspects for the HIRAM project since its inception and have contributed to this work through various technical discussions. S. Palaniswamy and S. Chakravarthy of the Rockwell Science Center provided numerous points of technical assistance with the USA-RG code.

References

[1] Kruczynski, D. L., "Flow Visualization of Steady and Transient Combustion in a 120-MM Ram Accelerator," AIAA Paper 94-3344, June 1994.

[2] Kruczynski, D. L., "Experiments in a 120-MM Ram Accelerator Including Flow Visualization," *Proceedings of the 31st JANNAF Combustion Subcommittee Meeting*, CPIA Pub. 620, Vol. 1, 1994, pp. 102–110.

[3] Nusca, M. J., "Reacting Flow Simulation for a Large Scale Ram Accelerator," AIAA Paper 94-2963, June 1994.

[4] Nusca, M. J., "Numerical Simulation of Ram Accelerator Performance Including Transient Effects During Initiation of Combustion and Sensitivity Studies," *Proceedings of the 31st JANNAF Combustion Subcommittee Meeting*, CPIA Pub. 620, Vol. 1, 1994, pp. 111–118.

[5] Liberatore, F., "Ram Accelerator Performance Calculations Using a Modified Version of the NASA CET89 Equilibrium Chemistry Code," U.S. Army Research Lab., ARL-TR-647, Aberdeen Proving Ground, MD, Dec. 1994.

[6] Hertzberg, A., Bruckner, A. P., and Bogdanoff, D. W., "Ram Accelerator: A New Chemical Method for Accelerating Projectiles to Ultrahigh Velocities," *AIAA Journal*, Vol. 26, No. 2, 1988, pp. 195–203.

[7] Giraud, M., Legendre, J.-F., and Simon, G., "Ram Acceleration at ISL; First Experiments in 90mm Caliber," *Proceedings of the 42nd Meeting of the Aeroballistic Range Association*, Adelaide, Australia, 1991, pp. 12–16.

[8] Smeets, G., Seiler, F., Patz, G., and Srulijes, J., "First Results Obtained in a 30mm Caliber Scram Accelerator Using a Rail Tube For Cylindrical Projectiles," *Proceedings of the 25th International Symposium on Combustion* (Irvine, CA), Combustion Inst., Pittsburgh, PA, 1994, pp. 21–35.

[9] Chakravarthy, S. R., Szema, K. Y., Goldberg, U. C., Gorski, J. J., and Osher, S., "Application of a New Class of High Accuracy TVD Schemes to the Navier-Stokes Equations," AIAA Paper 85-0165, Jan. 1985.

[10] Palaniswamy, S., and Chakravarthy, S. R., "Finite Rate Chemistry for USA Series Codes: Formulation and Applications," AIAA Paper 89-0200, Jan. 1989.

[11] Palaniswamy, S., Ota, D. K., and Chakravarthy, S. R., "Some Reacting-Flow Validation Results for USA-Series Codes," AIAA Paper 91-0583, Jan. 1991.

[12] Roe, P. L., "Approximate Riemann Solvers, Parameter Vectors, and Difference Schemes," *Journal of Computational Physics*, Vol. 43, No. 2, 1981, pp. 357–372.

[13] Soetrisno, M., Imlay, S. T., and Roberts, D. W., "Numerical Simulations of the Transdetonative Ram Accelerator Combusting Flow Field on a Parallel Computer," AIAA Paper 92-3249, July 1992.

[14] Yunster, S., and Rabinowitz, M. J., "Computation of Shock-Induced Combustion Using a Detailed Methane-Air Mechanism," *Journal of Propulsion and Power*, Vol. 10, No. 5, 1994, pp. 609–617.

[15] Li, C., Landsberg, A. M., Kailasanath, K., Oran, E. S., and Boris, J. P., "Numerical Simulations of Reactive Flows in Ram Accelerators," *Proceedings of the 29th JANNAF Combustion Meeting*, CPIA Pub. 593, Vol. 1, 1992, pp. 279–288.

[16] Hosangadi, A., York, B. J., Sinha, N., and Dash, S. M., "Progress in Transient Interior Ballistic Flowfield Simulations Using Multi-Dimensional Upwind/Implicit Numerics," AIAA Paper 93-1915, June 1993.

[17]Stull, D. R., and Prophet, H., "JANNAF Thermochemical Tables," 2nd ed., National Bureau of Standards, NSRDS-Rept. 37, June 1971.

[18]Wilke, C. R., "A Viscosity Equation for Gas Mixtures," *Journal of Chemistry and Physics*, Vol. 18, No. 4, 1950, pp. 517–519.

[19]Drummond, J. P., Rogers, C., and Hussaini, M. Y., "A Numerical Model for Supersonic Reacting Mixing Layer," *Computer Methods in Applied Mechanics and Engineering*, Vol. 64, No. 1, 1987, pp. 16–32.

[20]Gruschka, H. D., and Wecken, F., *Gasdynamic Theory of Detonation*, Gordon and Breach, New York, 1971.

[21]Reif, F., *Fundamentals of Statistical and Thermal Physics*, McGraw–Hill, New York, 1965.

[22]Smith, J. M., and Van Ness, H. C., *Introduction to Chemical Engineering Thermodynamics*, 4th ed., McGraw–Hill, New York, 1987.

[23]Smith, W., and Missen, R., *Chemical Reaction Equilibrium Analysis*, Wiley, New York, 1982.

[24]Hirschfelder, J. O., Curtiss, C. F., and Bird, R., *Molecular Theory of Gases and Liquids*, Wiley, New York, 1954.

[25]Anderson, D. A., Tannehill, J. C., and Pletcher, R. H., *Computational Fluid Mechanics and Heat Transfer*, Hemisphere, McGraw–Hill, New York, 1984.

[26]Baldwin, B. S., and Lomax, H., "Thin Layer Approximation and Algebraic Model for Separated Turbulent Flows," AIAA Paper 78-257, Jan. 1978.

[27]Goldberg, U. C., "Separated Flow Treatment with a New Turbulence Model," *AIAA Journal*, Vol. 24, No. 10, 1986, pp. 1711–1713.

[28]Westbrook, C. K., and Dryer, F. L., "Simplified Reaction Mechanisms for the Oxidation of Hydrocarbon Fuels in Flames," *Combustion Science and Technology*, Vol. 27, No. 1, 1981, pp. 31–43.

[29]Anderson, W. R., and Kotlar, A. J., "Detailed Modeling of CH_4/O_2 Combustion for Hybrid In-Bore Ram Propulsion (HIRAM) Application," *Proceedings of the 28th JANNAF Combustion Meeting*, CPIA Pub. 573, Vol. 2, 1991, pp. 417–426.

[30]Westbrook, C. K., and Dryer, F. L., "Chemical Kinetic Modeling of Hydrocarbon Combustion," *Progress in Energy Combustion Science*, Vol. 10, No. 1, 1984, pp. 1–57.

[31]Kruczynski, D. L., Liberatore, F., and Nusca, M. J., "Experimental Flow Visualization for a Large Scale Ram Accelerator," *Journal of Propulsion and Power*, Vol. 12, No. 1, 1996, pp. 206–209.